

Seasonal Variations of the Atmospheric Muon Neutrino Spectrum measured with IceCube

R. Abbasi¹⁷, M. Ackermann⁶⁵, J. Adams¹⁸, S. K. Agarwalla^{40,a}, J. A. Aguilar¹¹, M. Ahlers²², J.M. Alameddine²³, N. M. Amin⁴⁴, K. Andeen⁴², C. Argüelles¹⁴, Y. Ashida⁵³, S. Athanasiadou⁶⁵, S. N. Axani⁴⁴, R. Babu²⁴, X. Bai⁵⁰, A. Balagopal V.⁴⁰, M. Baricevic⁴⁰, S. W. Barwick³⁰, S. Bash²⁷, V. Basu⁴⁰, R. Bay⁷, J. J. Beatty^{20,21}, J. Becker Tjus^{10,b}, J. Beise⁶³, C. Bellenghi²⁷, S. BenZvi⁵², D. Berley¹⁹, E. Bernardini⁴⁸, D. Z. Besson³⁶, E. Blaufuss¹⁹, L. Bloom⁶⁰, S. Blot⁶⁵, F. Bontempo³¹, J. Y. Book Motzkin¹⁴, C. Boscolo Meneguolo⁴⁸, S. Böser⁴¹, O. Botner⁶³, J. Böttcher¹, J. Braun⁴⁰, B. Brinson⁵, Z. Brisson-Tsavoussis³³, J. Brostean-Kaiser⁶⁵, L. Brusa¹, R. T. Burley², D. Butterfield⁴⁰, M. A. Campana⁴⁹, I. Caracas⁴¹, K. Carloni¹⁴, J. Carpio^{34,35}, S. Chattopadhyay^{40,a}, N. Chau¹¹, Z. Chen⁵⁶, D. Chirkin⁴⁰, S. Choi^{57,58}, B. A. Clark¹⁹, A. Coleman⁶³, P. Coleman¹, G. H. Collin¹⁵, A. Connolly^{20,21}, J. M. Conrad¹⁵, R. Corley⁵³, D. F. Cowen^{61,62}, C. De Clercq¹², J. J. DeLaunay⁶⁰, D. Delgado¹⁴, S. Deng¹, A. Desai⁴⁰, P. Desiati⁴⁰, K. D. de Vries¹², G. de Wasseige³⁷, T. DeYoung²⁴, J. C. Díaz-Vélez⁴⁰, P. Dierichs¹, S. DiKerby²⁴, M. Dittmer⁴³, A. Domi²⁶, L. Draper⁵³, H. Dujmovic⁴⁰, D. Durnford²⁵, K. Dutta⁴¹, M. A. DuVernois⁴⁰, T. Ehrhardt⁴¹, L. Eidenschink²⁷, A. Eimer²⁶, P. Eller²⁷, E. Ellinger⁶⁴, S. El Mentawi¹, D. Elsässer²³, R. Engel^{31,32}, H. Erpenbeck⁴⁰, W. Esmail⁴³, J. Evans¹⁹, P. A. Evenson⁴⁴, K. L. Fan¹⁹, K. Fang⁴⁰, K. Farrag¹⁶, A. R. Fazely⁶, A. Fedynitch⁵⁹, N. Feigl⁹, S. Fiedlschuster²⁶, C. Finley⁵⁵, L. Fischer⁶⁵, D. Fox⁶¹, A. Franckowiak¹⁰, S. Fukami⁶⁵, P. Fürst¹, J. Gallagher³⁹, E. Ganster¹, A. Garcia¹⁴, M. Garcia⁴⁴, G. Garg^{40,a}, E. Genton^{14,37}, L. Gerhardt⁸, A. Ghadimi⁶⁰, C. Girard-Carillo⁴¹, C. Glaser⁶³, T. Glüsenkamp⁶³, J. G. Gonzalez⁴⁴, S. Goswami^{34,35}, A. Granados²⁴, D. Grant¹³, S. J. Gray¹⁹, S. Griffin⁴⁰, S. Griswold⁵², K. M. Groth²², D. Guevel⁴⁰, C. Günther¹, P. Gutjahr²³, C. Ha⁵⁴, C. Haack²⁶, A. Hallgren⁶³, L. Halve¹, F. Halzen⁴⁰, L. Hamacher¹, H. Hamdaoui⁵⁶, M. Ha Minh²⁷, M. Handt¹, K. Hanson⁴⁰, J. Hardin¹⁵, A. A. Harnisch²⁴, P. Hatch³³, A. Haungs³¹, J. Häußler¹, K. Helbing⁶⁴, J. Hellrung¹⁰, J. Hermannsgabner¹, L. Heuermann¹, N. Heyer⁶³, S. Hickford⁶⁴, A. Hidvegi⁵⁵, C. Hill¹⁶, G. C. Hill², R. Hmaid¹⁶, K. D. Hoffman¹⁹, S. Hori⁴⁰, K. Hoshina^{40,c}, M. Hostert¹⁴, W. Hou³¹, T. Huber³¹, K. Hultqvist⁵⁵, M. Hünnefeld⁴⁰, R. Hussain⁴⁰, K. Hymon^{23,59}, A. Ishihara¹⁶, W. Iwakiri¹⁶, M. Jacquart⁴⁰, S. Jain⁴⁰, O. Janik²⁶, M. Jansson⁵⁷, M. Jeong⁵³, M. Jin¹⁴, B. J. P. Jones⁴, N. Kamp¹⁴, D. Kang³¹, W. Kang⁵⁷, X. Kang⁴⁹, A. Kappes⁴³, D. Kappesser⁴¹, L. Kardum²³, T. Karg⁶⁵, M. Karl²⁷, A. Karle⁴⁰, A. Katil²⁵, U. Katz²⁶, M. Kauer⁴⁰, J. L. Kelley⁴⁰, M. Khanal⁵³, A. Khattee Zathul⁴⁰, A. Kheirandish^{34,35}, J. Kiryluk⁵⁶, S. R.

Klein^{7,8}, Y. Kobayashi¹⁶, A. Kochocki²⁴, R. Koirala⁴⁴, H. Kolanoski⁹, T. Kontrimas²⁷, L. Köpke⁴¹, C. Kopper²⁶, D. J. Koskinen²², P. Koundal⁴⁴, M. Kowalski^{9,65}, T. Kozynets²², N. Krieger¹⁰, J. Krishnamoorthi^{40,a}, T. Krishnan¹⁴, K. Kruiswijk³⁷, E. Krupczak²⁴, A. Kumar⁶⁵, E. Kun¹⁰, N. Kurahashi⁴⁹, N. Lad⁶⁵, C. Lagunas Gualda²⁷, M. Lamoureux³⁷, M. J. Larson¹⁹, F. Lauber⁶⁴, J. P. Lazar³⁷, K. Leonard DeHolton⁶², A. Leszczyńska⁴⁴, J. Liao⁵, M. Lincetto¹⁰, Y. T. Liu⁶², M. Liubarska²⁵, C. Love⁴⁹, L. Lu⁴⁰, F. Lucarelli²⁸, W. Luszczak^{20,21}, Y. Lyu^{7,8}, J. Madsen⁴⁰, E. Magnus¹², K. B. M. Mahn²⁴, Y. Makino⁴⁰, E. Manao²⁷, S. Mancina⁴⁸, A. Mand⁴⁰, W. Marie Sainte⁴⁰, I. C. Mariş¹¹, S. Marka⁴⁶, Z. Marka⁴⁶, M. Marsee⁶⁰, I. Martinez-Soler¹⁴, R. Maruyama⁴⁵, F. Mayhew²⁴, F. McNally³⁸, J. V. Mead²², K. Meagher⁴⁰, S. Mechbal⁶⁵, A. Medina²¹, M. Meier¹⁶, Y. Merckx¹², L. Merten¹⁰, J. Mitchell⁶, L. Molchany⁵⁰, T. Montaruli²⁸, R. W. Moore²⁵, Y. Morii¹⁶, R. Morse⁴⁰, M. Moulai⁴⁰, T. Mukherjee³¹, R. Naab⁶⁵, M. Nakos⁴⁰, U. Naumann⁶⁴, J. Necker⁶⁵, A. Negi⁴, L. Neste⁵⁵, M. Neumann⁴³, H. Niederhausen²⁴, M. U. Nisa²⁴, K. Noda¹⁶, A. Noell¹, A. Novikov⁴⁴, A. Obertacke Pollmann¹⁶, V. O'Dell⁴⁰, A. Olivas¹⁹, R. Orsoe²⁷, J. Osborn⁴⁰, E. O'Sullivan⁶³, V. Palusova⁴¹, H. Pandya⁴⁴, N. Park³³, G. K. Parker⁴, V. Parrish²⁴, E. N. Paudel⁴⁴, L. Paul⁵⁰, C. Pérez de los Heros⁶³, T. Pernice⁶⁵, J. Peterson⁴⁰, A. Pizzuto⁴⁰, M. Plum⁵⁰, A. Pontén⁶³, Y. Popovych⁴¹, M. Prado Rodriguez⁴⁰, B. Pries²⁴, R. Procter-Murphy¹⁹, G. T. Przybylski⁸, L. Pyras⁵³, C. Raab³⁷, J. Rack-Helleis⁴¹, N. Rad⁶⁵, M. Ravn⁶³, K. Rawlins³, Z. Rechav⁴⁰, A. Rehman⁴⁴, I. Reistroffer⁵⁰, E. Resconi²⁷, S. Reusch⁶⁵, W. Rhode²³, B. Riedel⁴⁰, A. Rifaie⁶⁴, E. J. Roberts², S. Robertson^{7,8}, S. Rodan^{57,58}, M. Rongen²⁶, A. Rosted¹⁶, C. Rott^{53,57}, T. Ruhe²³, L. Ruohan²⁷, I. Safa⁴⁰, J. Saffer³², D. Salazar-Gallegos²⁴, P. Sampathkumar³¹, A. Sandrock⁶⁴, M. Santander⁶⁰, S. Sarkar²⁵, S. Sarkar⁴⁷, J. Savelberg¹, P. Savina⁴⁰, P. Schaile²⁷, M. Schaufel¹, H. Schieler³¹, S. Schindler²⁶, L. Schlickmann⁴¹, B. Schlüter⁴³, F. Schlüter¹¹, N. Schmeisser⁶⁴, T. Schmidt¹⁹, J. Schneider²⁶, F. G. Schröder^{31,44}, L. Schumacher²⁶, S. Schwirn¹, S. Sclafani¹⁹, D. Seckel⁴⁴, L. Seen⁴⁰, M. Seikh³⁶, M. Seo⁵⁷, S. Seunarine⁵¹, P. A. Sevre Myhr³⁷, R. Shah⁴⁹, S. Shefali³², N. Shimizu¹⁶, M. Silva⁴⁰, B. Skrzypek⁷, B. Smithers⁴, R. Snihur⁴⁰, J. Soedingrekso²³, A. Søgaaard²², D. Soldin⁵³, P. Soldin¹, G. Sommani¹⁰, C. Spannfellner²⁷, G. M. Spiczak⁵¹, C. Spiering⁶⁵, J. Stachurska²⁹, M. Stamatikos²¹, T. Stanev⁴⁴, T. Stezelberger⁸, T. Stürwald⁶⁴, T. Stuttard²², G. W. Sullivan¹⁹, I. Taboada⁵, S. Ter-Antonyan⁶, A. Terliuk²⁷, A. Thakuri⁵⁰, M. Thiesmeyer⁴⁰, W. G. Thompson¹⁴, J. Thwaites⁴⁰, S. Tilav⁴⁴, K. Tollefson²⁴, C. Tönnis⁵⁷, S. Toscano¹¹, D. Tosi⁴⁰, A. Trettin⁶⁵, M. A. Unland Elorrieta⁴³, A. K. Upadhyay^{40,a}, K. Upshaw⁶, A. Vaidyanathan⁴², N. Valtonen-Mattila⁶³, J. Vandenbroucke⁴⁰, N. van Eijndhoven¹², D. Vannerom¹⁵, J. van Santen⁶⁵, J. Vara⁴³, F. Varsi³², J. Veitch-Michaelis⁴⁰, M. Venugopal³¹, M. Vereecken³⁷, S. Vergara Carrasco¹⁸, S. Verpoest⁴⁴, D. Veske⁴⁶, A. Vijai¹⁹, C. Walck⁵⁵, A. Wang⁵, C. Weaver²⁴, P.

Weigel¹⁵, A. Weindl³¹, J. Weldert⁶², A. Y. Wen¹⁴, C. Wendt⁴⁰,
 J. Werthebach²³, M. Weyrauch³¹, N. Whitehorn²⁴, C. H.
 Wiebusch¹, D. R. Williams⁶⁰, L. Witthaus²³, M. Wolf²⁷, G.
 Wrede²⁶, X. W. Xu⁶, J. P. Yanez²⁵, E. Yildizci⁴⁰, S. Yoshida¹⁶,
 R. Young³⁶, F. Yu¹⁴, S. Yu⁵³, T. Yuan⁴⁰, A. Zegarelli¹⁰,
 S. Zhang²⁴, Z. Zhang⁵⁶, P. Zhelnin¹⁴, P. Zilberman⁴⁰, M.
 Zimmerman⁴⁰

¹III. Physikalisches Institut, RWTH Aachen University, D-52056 Aachen, Germany

²Department of Physics, University of Adelaide, Adelaide, 5005, Australia

³Dept. of Physics and Astronomy, University of Alaska Anchorage, 3211 Providence Dr., Anchorage, AK 99508, USA

⁴Dept. of Physics, University of Texas at Arlington, 502 Yates St., Science Hall Rm 108, Box 19059, Arlington, TX 76019, USA

⁵School of Physics and Center for Relativistic Astrophysics, Georgia Institute of Technology, Atlanta, GA 30332, USA

⁶Dept. of Physics, Southern University, Baton Rouge, LA 70813, USA

⁷Dept. of Physics, University of California, Berkeley, CA 94720, USA

⁸Lawrence Berkeley National Laboratory, Berkeley, CA 94720, USA

⁹Institut für Physik, Humboldt-Universität zu Berlin, D-12489 Berlin, Germany

¹⁰Fakultät für Physik & Astronomie, Ruhr-Universität Bochum, D-44780 Bochum, Germany

¹¹Université Libre de Bruxelles, Science Faculty CP230, B-1050 Brussels, Belgium

¹²Vrije Universiteit Brussel (VUB), Dienst ELEM, B-1050 Brussels, Belgium

¹³Dept. of Physics, Simon Fraser University, Burnaby, BC V5A 1S6, Canada

¹⁴Department of Physics and Laboratory for Particle Physics and Cosmology, Harvard University, Cambridge, MA 02138, USA

¹⁵Dept. of Physics, Massachusetts Institute of Technology, Cambridge, MA 02139, USA

¹⁶Dept. of Physics and The International Center for Hadron Astrophysics, Chiba University, Chiba 263-8522, Japan

¹⁷Department of Physics, Loyola University Chicago, Chicago, IL 60660, USA

¹⁸Dept. of Physics and Astronomy, University of Canterbury, Private Bag 4800, Christchurch, New Zealand

¹⁹Dept. of Physics, University of Maryland, College Park, MD 20742, USA

²⁰Dept. of Astronomy, Ohio State University, Columbus, OH 43210, USA

²¹Dept. of Physics and Center for Cosmology and Astro-Particle Physics, Ohio State University, Columbus, OH 43210, USA

²²Niels Bohr Institute, University of Copenhagen, DK-2100 Copenhagen, Denmark

²³Dept. of Physics, TU Dortmund University, D-44221 Dortmund, Germany

²⁴Dept. of Physics and Astronomy, Michigan State University, East Lansing, MI 48824, USA

²⁵Dept. of Physics, University of Alberta, Edmonton, Alberta, T6G 2E1, Canada

²⁶Erlangen Centre for Astroparticle Physics, Friedrich-Alexander-Universität Erlangen-Nürnberg, D-91058 Erlangen, Germany

²⁷Physik-department, Technische Universität München, D-85748 Garching, Germany

²⁸Département de physique nucléaire et corpusculaire, Université de Genève, CH-1211 Genève, Switzerland

²⁹Dept. of Physics and Astronomy, University of Gent, B-9000 Gent, Belgium

³⁰Dept. of Physics and Astronomy, University of California, Irvine, CA 92697, USA

³¹Karlsruhe Institute of Technology, Institute for Astroparticle Physics, D-76021 Karlsruhe, Germany

³²Karlsruhe Institute of Technology, Institute of Experimental Particle Physics, D-76021 Karlsruhe, Germany

³³Dept. of Physics, Engineering Physics, and Astronomy, Queen's University, Kingston, ON K7L 3N6, Canada

³⁴Department of Physics & Astronomy, University of Nevada, Las Vegas, NV 89154, USA

³⁵Nevada Center for Astropysics, University of Nevada, Las Vegas, NV 89154, USA

³⁶Dept. of Physics and Astronomy, University of Kansas, Lawrence, KS 66045, USA

³⁷Centre for Cosmology, Particle Physics and Phenomenology - CP3, Université catholique de Louvain, Louvain-la-Neuve, Belgium

³⁸Department of Physics, Mercer University, Macon, GA 31207-0001, USA

³⁹Dept. of Astronomy, University of Wisconsin—Madison, Madison, WI 53706, USA

⁴⁰Dept. of Physics and Wisconsin IceCube Particle Astrophysics Center, University of Wisconsin—Madison, Madison, WI 53706, USA

USA

⁴¹Institute of Physics, University of Mainz, Staudinger Weg 7, D-55099 Mainz, Germany

⁴²Department of Physics, Marquette University, Milwaukee, WI 53201, USA

⁴³Institut für Kernphysik, Universität Münster, D-48149 Münster, Germany

⁴⁴Bartol Research Institute and Dept. of Physics and Astronomy, University of Delaware, Newark, DE 19716, USA

⁴⁵Dept. of Physics, Yale University, New Haven, CT 06520, USA

⁴⁶Columbia Astrophysics and Nevis Laboratories, Columbia University, New York, NY 10027, USA

⁴⁷Dept. of Physics, University of Oxford, Parks Road, Oxford OX1 3PU, United Kingdom

⁴⁸Dipartimento di Fisica e Astronomia Galileo Galilei, Università Degli Studi di Padova, I-35122 Padova PD, Italy

⁴⁹Dept. of Physics, Drexel University, 3141 Chestnut Street, Philadelphia, PA 19104, USA

⁵⁰Physics Department, South Dakota School of Mines and Technology, Rapid City, SD 57701, USA

⁵¹Dept. of Physics, University of Wisconsin, River Falls, WI 54022, USA

⁵²Dept. of Physics and Astronomy, University of Rochester, Rochester, NY 14627, USA

⁵³Department of Physics and Astronomy, University of Utah, Salt Lake City, UT 84112, USA

⁵⁴Dept. of Physics, Chung-Ang University, Seoul 06974, Republic of Korea

⁵⁵Oskar Klein Centre and Dept. of Physics, Stockholm University, SE-10691 Stockholm, Sweden

⁵⁶Dept. of Physics and Astronomy, Stony Brook University, Stony Brook, NY 11794-3800, USA

⁵⁷Dept. of Physics, Sungkyunkwan University, Suwon 16419, Republic of Korea

⁵⁸Institute of Basic Science, Sungkyunkwan University, Suwon 16419, Republic of Korea

⁵⁹Institute of Physics, Academia Sinica, Taipei, 11529, Taiwan

⁶⁰Dept. of Physics and Astronomy, University of Alabama, Tuscaloosa, AL 35487, USA

⁶¹Dept. of Astronomy and Astrophysics, Pennsylvania State University, University Park, PA 16802, USA

⁶²Dept. of Physics, Pennsylvania State University, University Park, PA 16802, USA

⁶³Dept. of Physics and Astronomy, Uppsala University, Box 516, SE-75120 Uppsala, Sweden

⁶⁴Dept. of Physics, University of Wuppertal, D-42119 Wuppertal, Germany

⁶⁵Deutsches Elektronen-Synchrotron DESY, Platanenallee 6, D-15738 Zeuthen, Germany

Received: date / Accepted: date

^aalso at Institute of Physics, Sachivalaya Marg, Sainik School Post, Bhubaneswar 751005, India

^balso at Department of Space, Earth and Environment, Chalmers University of Technology, 412 96 Gothenburg, Sweden

^calso at Earthquake Research Institute, University of Tokyo, Bunkyo, Tokyo 113-0032, Japan

^de-mail: analysis@icecube.wisc.edu

Abstract This study presents an energy-dependent analysis of seasonal variations in the atmospheric muon neutrino spectrum, using 11.3 years of data from the IceCube Neutrino Observatory. By leveraging a novel spectral unfolding method, we explore the energy range from 125 GeV to 10 TeV for zenith angles between 90° to 110° , corresponding to the Antarctic atmosphere. Our findings reveal that the seasonal variation amplitude decreases with energy reaching $(-4.6 \pm 1.1)\%$ during Austral winter and increases $(+3.9 \pm 1.2)\%$ during Austral summer relative to the annual average at 10 TeV. While the unfolded flux exceeds the model predictions by up to 30%, the differential measurement of seasonal variations remains unaffected. The measured seasonal variations of the muon neutrino spectrum are consistent with theoretical predictions using the MCEq code and the NRLMSISE-00 atmospheric model.

Keywords Atmospheric neutrinos · seasonal variations · unfolding · IceCube

1 Introduction

Atmospheric leptons, such as muons, muon neutrinos, and electron neutrinos, originate from highly relativistic meson decays, mainly from kaons and pions, within cosmic-ray-induced particle cascades (air showers) [1]. If the interaction length λ_{int} of a parent meson exceeds its decay length λ_{dec} , the particle is more likely to decay before undergoing an inelastic collision. In the case of a charged pion, it will distribute its entire energy between a muon and a muon neutrino. Conversely, if $\lambda_{\text{int}} \ll \lambda_{\text{dec}}$, a parent meson will more likely interact inelastically with an air nucleus, lower-energy mesons and decay products are produced, which results in a steeper atmospheric lepton spectrum. This transition occurs around the critical energy of approximately $115 \text{ GeV} / \cos \theta^*$ for charged pions and $850 \text{ GeV} / \cos \theta^*$ for charged kaons, with θ^* measured perpendicularly to the top of the atmosphere h at the point of the cosmic ray's entrance, as illustrated in Fig. 1.

Atmospheric density and temperature are critical parameters in this process. Seasonal temperature variations in the upper thermosphere and lower stratosphere affect the atmospheric density gradient. An increase in atmospheric density, coupled with a decrease in temperature, shortens the interaction length and reduces the probability of meson decay before an inelastic collision. While the interaction length depends on the slant depth X , measured in g/cm^2 , defined as the integral of the density ρ along the line l of sight $X = \int_l^\infty dl' \rho(l')$, the decay length explicitly depends on the density at a specific slant depth (see Fig. 1). This results in a modulation

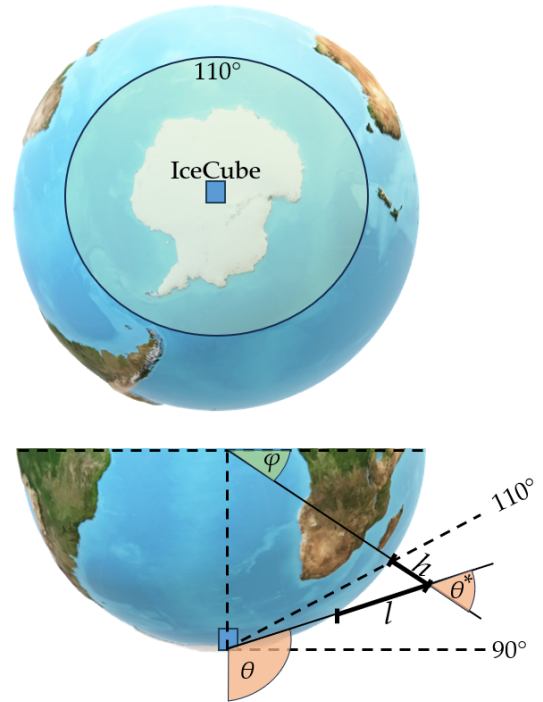


Fig. 1 Illustration of the experimental setup. The upper figure depicts the atmospheric region, the Antarctic atmosphere, in which the neutrinos from the event selection are produced, and the IceCube detector at the South Pole. The illustration at the bottom shows the definition of relevant physical quantities and the zenith region to be analyzed in IceCube coordinates θ . The path of the neutrino along the line of sight is given by l , the vertical height by h . The spanned zenith region in the bottom figure is not to scale.

of the critical energy, which in turn alters the energy at which the spectral index changes. Consequently, the integral event rate of muons and neutrinos depends on the variations of atmospheric conditions, and a reduced critical energy results in a decreased flux of high-energy leptons.

Variations in atmospheric conditions and their impact on air showers can be investigated using neutrinos and muons. The measurement of seasonal variations in the muon flux is well-established for underground particle observatories [2, 3, 4, 5, 6, 7, 8, 9, 10]. In contrast, measuring seasonal variations in the atmospheric neutrino flux poses significant challenges due to the limited event rate and substantial background from cosmic ray muons. The IceCube detector mitigates this challenge by being shielded from muons by the Earth when observing in the northerly direction (see Fig. 1), while neutrinos, capable of penetrating the Earth, can reach the detector from all directions. The effect of seasonal variations provides information on the K/π -ratio, due to the difference in the critical energy of these mesons [11, 12]. Whereas variations in the muon flux variations

are predominantly due to pions, variations in the neutrino flux are primarily driven by contributions from both pions and kaons [13]. Determining seasonal variations in the neutrino flux can constrain kaon production in air showers, a major source of uncertainty in atmospheric neutrino flux predictions [14, 15]. Furthermore, these measurements probe a larger atmospheric region compared to muon-based observations in IceCube and provide critical background estimates for astrophysical neutrino searches. Using six years of experimental data from the IceCube Neutrino Observatory, the amplitude of seasonal variations in the atmospheric neutrino flux and its correlation with temperature were determined in [16] as proposed in [17, 18].

This study presents a measurement of the seasonal variations of the muon neutrino energy spectrum using 11.3 years of data from the IceCube Neutrino Observatory, effectively doubling the size of the data set used previously in [16]. The increased event count allows us to analyze seasonal variations in the energy spectrum with a spectrum unfolding method.

This paper is structured as follows. The energy-dependence of seasonal variations is discussed in Section 2, the IceCube Neutrino Observatory and the event selection are introduced in Section 3. Section 4 presents the seasonal variation observed in the event rate in IceCube. The spectrum unfolding method is introduced in Section 5 with the final results presented in Section 6.

2 Seasonal variations of atmospheric neutrinos

The energy-dependence of seasonal variations in the atmospheric muon neutrino flux, the variation in production heights, and the impacts of kaon and pion contribution to these variations are not extensively discussed in the literature. Therefore, we briefly summarize the physical principles underlying the seasonal variations of atmospheric neutrinos in this section.

2.1 Theoretical modeling

The Matrix-Cascade Equations (MCEq) code [19, 13] is a numerical solver of the one-dimensional relativistic transport equations (cascade equations) for particles propagating through dense or gaseous media, such as the Earth's atmosphere. MCEq iteratively calculates the evolution of the individual spectra of secondary particles produced through hadronic interactions or decays as a function of the slant depth in the atmosphere. The main required inputs are a model for the spectrum of primary cosmic rays at the top of the atmosphere, a model for the atmosphere's density, and a parameterization of the

cross section for inclusive particle production and decays. At energies above 10 GeV, low-energy effects such as solar modulation, deflections in the Earth's magnetic field can be safely neglected.

In this work, the initial cosmic ray flux is parameterized by the H3a [20] model, and SIBYLL-2.3c [13, 21] is used as the hadronic interaction model for all comparisons within this paper.

We test three different atmospheric density models. The default in MCEq for the location of the South Pole is the numerical representation of the NRLMSISE-00 model [22]. It is an empirical static atmospheric model that integrates a comprehensive array of measurements, including satellite data from the Atmospheric Explorer and Dynamics Explorer and ground-based observations. It combines data from mass spectrometers, accelerometers, and other instruments to precisely represent atmospheric temperature, density, and composition from the Earth's surface to the exosphere. The calculation of atmospheric cascades in MCEq extends to heights of 112.8 km.

We also tested two parameterizations from [16] based on temperature measurements by the Atmospheric Infrared Sounder (AIRS) [23] and by the European Centre for Medium-Range Weather Forecasts (ECMWF) [24], which includes an interpolation model of data taken by other instruments. The AIRS instrument orbits the Earth daily, resulting in 14×2 measurements per day. The temperature across the different positions around Earth are determined for 24 pressure levels ranging from 1000 hPa to 1 hPa, providing an angular resolution of $1^\circ \times 1^\circ$ in both latitude and longitude. Multiple gaps and missing data points exist due to the limited swath size and calibration processes in which the instrument cannot take data. These gaps are filled by interpolating the previous and consecutive measurement. The temperature profiles are converted into density, assuming the ideal gas equation. These density profiles are inputs for MCEq to obtain the daily forecast of the atmospheric neutrino rate from April 2012 to April 2017, which is then averaged into monthly rates. The ECMWF parameterization is based on the ERA-5 reanalysis dataset covering data from April 2012 to 2013. Due to limited statistical power, we cannot clearly distinguish the year-to-year variations of monthly neutrino rates. Therefore, the periods of the AIRS and ECMWF parameterizations are calculated as an average across the years, as atmospheric temperature variations at the South Pole are dominated by an annual cycle.

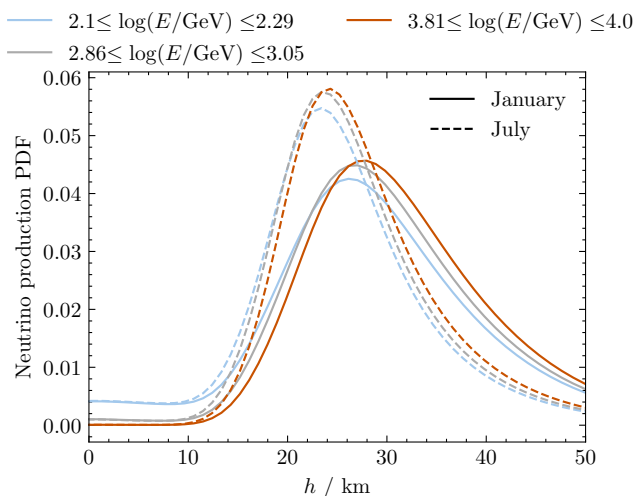


Fig. 2 Neutrino production profiles for January 1st (solid) and July 1st (dashed) calculated for the neutrino sample from the IceCube Neutrino Observatory, integrated over the zenith range from 90° to 110° calculated using MCEq with the NRLMSISE-00 atmospheric model. The analysis of seasonal variations is conducted in the energy range from 125 GeV to 10 TeV divided into ten equidistant logarithmic energy bins. The profiles in this figure are displayed for the first, fifth and highest energy bin.

2.2 Neutrino production in the Antarctic atmosphere

The atmospheric region to be investigated corresponds to horizontally arriving neutrinos at the IceCube Neutrino Observatory at the South Pole, shown in the upper part of Fig. 1. The lower part illustrates the geometry of the arriving neutrinos at the detector. The Antarctic atmosphere is characterized by a persistent and large-scale cyclone above continental Antarctica and parts of the Southern Ocean centered near the pole, referred to as a polar vortex, which extends into the troposphere and the stratosphere [25]. The polar vortex strengthens in winter and weakens in summer. The stratospheric vortex is located at altitudes between 10 km to 50 km, driven by the temperature gradient between the Equator and the poles. The clockwise winds confine cold air within the vortex, preventing it from mixing with the warmer surrounding air. The polar vortex remains confined until the heating of the stratosphere starts in August/September, triggered by the sunrise above Antarctica. Sudden stratospheric warmings can cause the vortex to break, splitting it into two parts, during which temperatures can rise dramatically – by up to 60 K in the stratosphere within a week. This effect has been observed using muons in IceCube [7].

The production profiles for neutrinos that pass the event selection in the analyzed dataset, introduced in Section 3.2, are obtained by calculating neutrino spec-

tra $\Phi_{\nu_\mu + \bar{\nu}_\mu}(E, h)$ with MCEq in steps of slant depth X and altitude h . These spectra are then folded with the effective areas [26] to derive event rates N_j in each energy bin, which are subsequently numerically integrated and normalized to a production profile probability density function. The integration over the solid angle has been done by computing effective areas and neutrino fluxes and summing over five equidistant zenith bins in $\cos(\theta)$ covering the analysis angular range from $\theta = 90^\circ$ to 110° .

As shown in Fig. 2 for the first, fifth and last energy bin within the analyzed range from 125 GeV to 10 TeV (introduced in Section 5.2), neutrino production mainly occurs at altitudes from 15 km to 50 km, within the polar vortex.

During Austral winter, represented by July 1, the production profiles are narrower due to the denser atmosphere. In this season, 90% of neutrinos in the first energy bin ($2.1 \leq \log(E/\text{GeV}) \leq 2.29$) are produced above 16.1 km, with peak production occurring at altitudes between 23 km to 24 km. For the highest energy bin ($3.81 \leq \log(E/\text{GeV}) \leq 4.0$), 90% of neutrinos are produced above 18.9 km, and production peaks between 24 km to 25 km, similar to that of the fifth energy bin ($2.86 \leq \log(E/\text{GeV}) \leq 3.05$). Conversely, during Austral summer, the atmosphere expands, leading to higher-altitude production. For the lowest energy bin, 90% of neutrinos are produced at altitudes above 17.0 km, and for the highest energy bin above 20.7 km, with substantial production above 30 km. Production peaks range between 24 km to 28 km for the first energy bin and between 26 km to 30 km for the highest energy bin. At altitudes below 10 km, production at energies below a few TeV is attributed primarily to neutrinos from muon decay (see Fig. 3).

It can be noted that the neutrino production height is energy-dependent with higher-energy neutrinos being produced at higher altitudes. The energy dependence is more pronounced in Austral summer, as indicated by the wider production profiles, suggesting a more complex correlation with seasonal temperature variations across altitude.

2.3 Expected seasonal variations of the atmospheric neutrino rate and the spectrum

The expected atmospheric muon neutrino flux according to a parent particle in the zenith range from 90° to 110° is displayed in Fig. 3 for two seasons, represented by January 1 and July 1. Below their critical energies, the pion and kaon components—referred to as the *conventional* neutrino flux—show minimal seasonal variations. In contrast, neutrinos from muon decay—originating

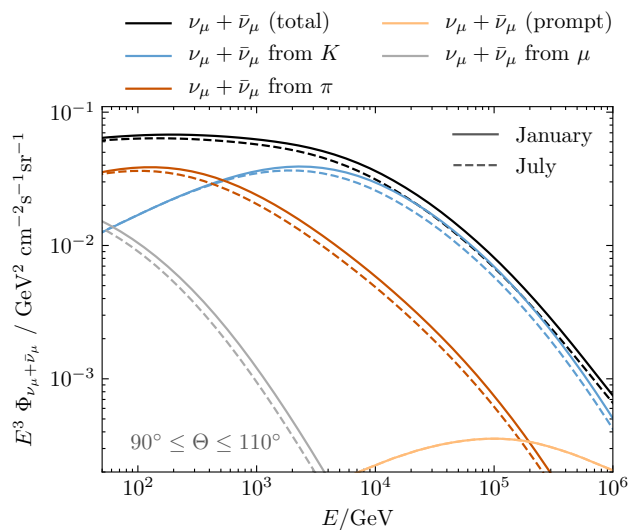


Fig. 3 Neutrino spectrum calculated with MCEq, showing contributions from parent particles for two seasons, January 1 and July 1. The seasonal differences in the total spectrum increase with energy above the critical energy of the respective parent particle. The prompt flux component does not show seasonal differences because of its critical energy exceeding the displayed energy range.

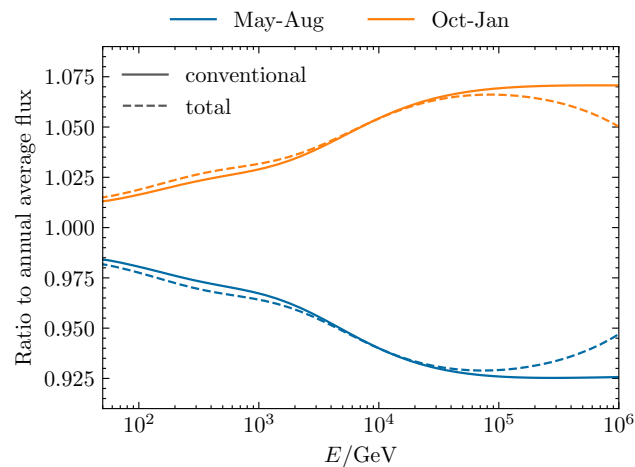


Fig. 4 The calculated ratio of the seasonal muon neutrino flux to the annual average, using MCEq with NRLMSISE-00 as the atmospheric density model, for the zenith range from 90° to 110° during Austral summer and winter. The total flux, including the prompt component, is shown with dashed lines, while solid lines represent the conventional flux. The strength of seasonal variation is expected to decrease as prompt neutrinos dominate at energies above several 100 TeV.

from higher-energy pions—reflect the seasonal dependence of their parent particles. The *prompt* neutrino flux component from short-lived mesons remains unaffected by seasonal temperature changes due to the immediate decay of their parent particles, driven by their large critical energies above 10^7 GeV.

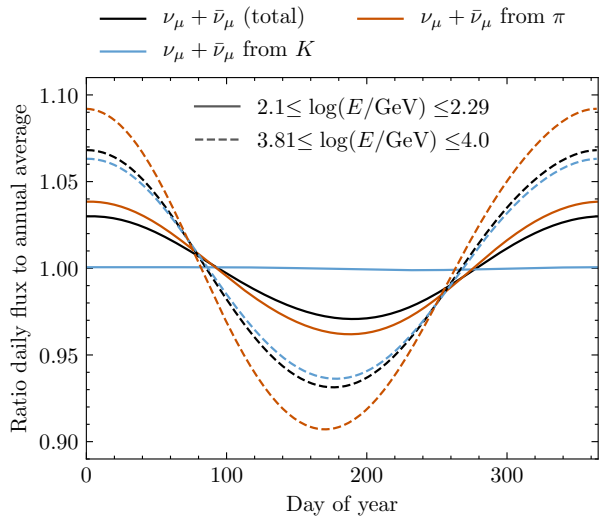


Fig. 5 Expected total neutrino rate variation per day of year relative to the annual average, calculated from the NRLMSISE-00 model for the zenith range from 90° to 110° . The solid line shows the rate derived for the lowest energy bin ($2.1 \leq \log(E/\text{GeV}) \leq 2.29$), while dashed lines show the rate for the highest energy bin ($3.81 \leq \log(E/\text{GeV}) \leq 4.0$). The rate variation is depicted for the total neutrino flux in black, while the contribution from kaons is shown in blue, and from pions in red. The seasonal variation in the first bin is dominated by pions. The contribution from kaons is compatible with the annual average as the energies are below the critical energy for kaons. The variations in the highest energy bin are mainly driven by kaons.

When the critical energy of the parent particles is exceeded, the spectrum becomes steeper with respect to the primary cosmic ray spectrum, as neutrino production is dominated by the reinteraction of their parent mesons. The prompt component only contributes substantially to the total flux above several 100 TeV, in particular at the horizon, flattening the total spectrum, which approximately follows the spectral index of the cosmic ray primary due to the immediate decay of the neutrino parents.

Fig. 4 shows the ratio of seasonal to annual average conventional and total muon neutrino flux for Austral summer and winter. As can be inferred from Fig. 3, the total flux below 500 GeV is dominated by the seasonal variation of neutrinos from pion decay. Above this energy, the amplitude of variations increases at a slower rate due to the growing contribution of kaons to the total flux, which exhibit smaller seasonal variations because of their higher critical energy. The amplitude increases more strongly above the critical energies of kaons due to the increasing seasonal dependence of the kaon flux. The amplitude approximately doubles around 10 TeV over two orders of magnitude in energy. The seasonal variation of the conventional component reaches its max-

imum amplitude above 100 TeV and remains constant. Below approximately 4 TeV, muon decay contributes to the seasonal variation, increasing the amplitude by up to 0.5% compared to the conventional flux variation. The total seasonal variation strength decreases above 60 TeV due to the increasing contribution of seasonally independent prompt neutrinos.

The amplitude of the variation strength of the lowest energy bin and the highest energy bin within the energy range of interest from 125 GeV to 10 TeV is shown in Fig. 5. For the first energy bin ($2.1 \leq \log(E/\text{GeV}) \leq 2.29$), the expected total amplitude is approximately $\pm 3\%$, primarily driven by variations in the pion component ($\pm 4\%$). The total variation amplitude is about 1% lower than the amplitude attributed to seasonal variations of pions due to the contribution of neutrinos originating from muon decay at energies below 1 TeV, as depicted in Fig. 3. The neutrino flux from kaons remains consistent with the annual average, as the critical energy has not yet been reached. In the highest energy bin ($3.81 \leq \log(E/\text{GeV}) \leq 4.0$), the amplitude is dominated by kaons, whereas the smaller contribution from pions increases the amplitude from $\pm 6.5\%$ (kaons) to $\pm 6.8\%$ (total). The subdominant contribution of neutrinos from pion decay are expected to show a variation amplitude more than $\pm 9\%$.

The variation phase shows a slightly slower decrease from day 0 to 180 governed by the presence of the polar vortex, followed by a slightly more rapid increase during the latter half of the year, with the lower energy bins dominated by neutrinos from pions and the higher bins by neutrinos from kaons. Differences in the timing of extrema and inflection points reflect temperature variations at different production altitudes. With sufficient statistics, seasonal variations could be more effectively used to constrain pion and kaon components in theoretical models in the future.

3 Data

3.1 The IceCube Neutrino Observatory

The IceCube Neutrino Observatory is a cubic-kilometer neutrino detector embedded in the glacial ice at the geographic South Pole [27]. The detection volume is instrumented by 5160 digital optical modules (DOMs) arranged on 86 cable strings on a hexagonal grid. A DOM consists of a photomultiplier tube in a pressure-resistant glass sphere and readout electronics. Neutrinos are detected indirectly via the Cherenkov light emitted by secondary particles created in interactions inside the ice or nearby bedrock. The IceCube detector is sensitive

to all neutrino flavors, which can be distinguished by their signature in the detector.

3.2 Event selection

The event selection follows [28], developed for the investigation of the astrophysical neutrino flux, as well as for the measurement of the correlation between seasonal variations of atmospheric neutrinos and temperature [16].

A significant background for selecting atmospheric neutrinos consists of atmospheric muons, which exceed the detection rate of atmospheric neutrinos by six orders of magnitude. However, the Earth is a natural shield against these muons, as they can only propagate through matter for a few kilometers at the energies relevant to this analysis. Consequently, only neutrino-induced muons can reach the detector in arrival directions with zenith angles $\gtrsim 90^\circ$, where the particle must enter from a horizontal direction or below, known as up-going events. The deep underground detector location provides additional shielding for zenith angles above 86° . In addition to selecting preferential arrival directions, the sample is further cleaned from the additional background of atmospheric muons and cascade events using two boosted decision trees, achieving 99.85% purity in the final event classification, as detailed in [29].

The measurement of seasonal variations is conducted only on a subset of events arriving within the zenith range from 90° to 110° , as depicted in Fig. 1. The sample, therefore, exclusively contains events from latitudes of the Southern Hemisphere with the most significant seasonal temperature changes across the globe. Larger zenith angles are excluded, as the seasonal temperature fluctuations in the stratosphere become too small towards the poles. The seasonal variations in the Northern Hemisphere are smaller in amplitude compared to the South, yielding smaller variations in the neutrino rate. The available statistics from the Arctic region is not yet large enough to conduct an energy-dependent seasonal analysis. Consequently, the neutrinos traversing the Earth and reaching the detector almost horizontally are particularly suitable for measuring seasonal variations in the neutrino flux due to the larger amplitude of temperature variations in the stratosphere and the characteristics of the polar vortex above Antarctica, as explained in Section 2.2, while retaining the natural shielding against atmospheric muons [16]. The selection of the zenith region is discussed in [30].

No distinction can be made between neutrinos of atmospheric or astrophysical origin for each event. However, the contribution of astrophysical neutrinos is negligible at energies below 10 TeV with less than 1% of

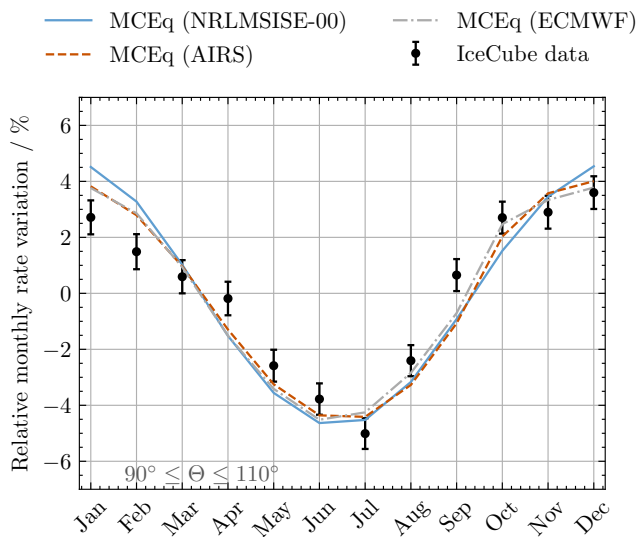


Fig. 6 Relative monthly muon neutrino rate in IceCube within the zenith range from 90° to 110° , averaged over the period from May 2011 to December 2022. Error bars represent the Poissonian uncertainty of the rate. The model expectations using three different parameterizations for the atmospheric density, described in more detail in Section 2.1, are shown in different linestyles.

the total neutrinos estimated to be of astrophysical origin. This analysis is conducted on 386,542 through-going neutrino-induced muons over 11.3 years of effective data-taking from May 2011 and December 2022.

4 Observed seasonal variation of the event rate

The observed monthly rate is determined by sorting data runs into months according to their start times within the data-taking period from May 2011 to December 2022, as explained in Section 3.2, including leap years. Subsequently, the variation of the average monthly rate is analyzed relatively to the annual average flux.

Fig. 6 shows the ratio of the monthly averages over the average annual neutrino rate. The measured ratio reaches its maximum during the Austral summer in December at $(+3.6 \pm 0.6)\%$, followed by a smooth decline from January to July, reaching a minimum of $(-5.0 \pm 0.6)\%$ in Austral winter. The observed transition from winter to summer amplitude is faster than the winter to summer transition due to the presence of the polar vortex, which confines cold air (discussed in Section 2.2).

The observed amplitude of the rate variation is in phase with the MCEq predictions with deviations in January, February, April, and September. The rate variation amplitudes calculated with the empirical model NRLMSISE-00 model are up to 1% larger in January and February, and about 1% lower in September and

October compared to the data-driven atmospheric parameterizations. A χ^2 -test incorporating only statistical uncertainties reveals a deviation of the observed rate from the calculation based on the NRLMSISE-00 model at 4.6σ . The parameterizations from AIRS and ECMWF describe the data slightly better, particularly during the Austral summer months and in October, with p-values corresponding to 3.1σ for AIRS and 2.7σ for ECMWF.

These findings are underlined by the analysis in [16], determined from data within the peak summer and winter months only. It is important to note that this comparison of observed rates with calculated predictions is based on monthly averages. Additionally, the calculation of rate variation from the atmospheric parameterizations does not account for measurement or model uncertainties. Deviations in spring and fall can be attributed to the modulation of the complex cooling and heating phases.

For the subsequent energy-dependent analysis, Austral summer and winter are defined as the periods with comparable amplitudes: October to January and May to August, respectively.

5 Spectrum unfolding

The true neutrino energy distribution $f(E)$ cannot be determined directly since neutrino energies are inferred from the measurement of Cherenkov photons produced by neutrino-induced muons. The relationship between the true energy distribution and the observed distribution $g(y)$ of measurable quantities y is described by the Fredholm integral equation of the first kind [31]:

$$g(y) = \int_a^b A(E, y) f(E) dE + b(y) + \epsilon(y). \quad (1)$$

$A(E, y)$ represents the detector response function that maps the true energy distribution. The additional terms $b(y)$ and $\epsilon(y)$ account for background contamination in the event selection and statistical/systematic uncertainties, respectively. Equation 1 is discretized due to the finite number of observations:

$$\vec{g}(y) = \mathbf{A}(x, y) \vec{f}(E) + \vec{b}(y) + \vec{\epsilon}(y). \quad (2)$$

Converting from measured quantities to the energy distribution constitutes an inverse problem, inherently ill-conditioned. The energy deposited by muons in the ice or nearby bedrock during their propagation is non-deterministic. At energies below 1 TeV, continuous losses dominate, while stochastic losses dominate at higher energies, contributing to the smearing of energy resolution.

Calculating particle propagation and energy losses relies on the lepton propagator PROPOSAL [32]. Spectrum unfolding addresses this ill-conditioned problem by estimating the true distribution from measured proxies obtained from a Monte Carlo detector response simulation.

5.1 Estimation of the energy spectrum

In this paper, we apply the DSEA algorithm to determine the neutrino energy spectrum for each season. Detailed information on the algorithm is provided in [33]. DSEA treats each energy bin (components of $\vec{f}(E)$) as described in Eq. 2) as a distinct class of events, effectively transforming the spectrum estimation problem into a multinomial classification task.

The binned energy spectrum \hat{f}_i is estimated through an iterative process. Initially, a random forest classifier is trained on energy-related features, discussed in the next section. This trained classifier predicts confidence scores $c_M(i | x_n)$ indicating the likelihood that each event x_n in the seasonal dataset belongs to energy bin index i .

The estimated content of each energy bin \hat{f}_i is calculated by

$$\hat{f}_i^{(k)} = \frac{1}{N_{\text{events}}} \sum_{n=1}^{N_{\text{events}}} c_M(i | x_n) \quad \forall 1 \leq i \leq I, \quad (3)$$

where the sum of the confidence scores is normalized to N_{events} events in the data set.

In the first iteration, the output is weighted to a uniform class distribution to mitigate potential bias in the trained model's class distribution. In subsequent iterations, the output is scaled by a variable step size, which regulates the convergence speed of the algorithm. The confidence scores from the random forest classifier are then weighted by the previous estimates. Detailed information about the algorithm is provided in [33].

5.2 Energy proxies

The neutrino energy is estimated from two reconstructed proxies: the number of hit DOMs per event, referred to as *number of DOMs*, and a likelihood reconstruction of the deposited energy along the muon trajectory through the detector, referred to as *truncated energy* ($E_{\text{truncated}}$) [34]. The correlation between these proxies and the true neutrino energy is shown in Fig. 7 for the energy range from 125 GeV to 10 TeV used in this analysis, including the median and the 68% quantiles.

The correlation of both quantities is smeared due to the unknown distance the muon traveled before entering the detector and the stochastic processes in muon propagation, as described above. This effect is highlighted in Fig. 8, which shows the correlation between the true neutrino energy and the true muon energy at the detector entry. Since the correlation is imperfect, the figure illustrates the complexity of estimating the neutrino energy from measurable detector quantities and highlights the necessity of an unfolding procedure to account for the smearing in the energy distribution.

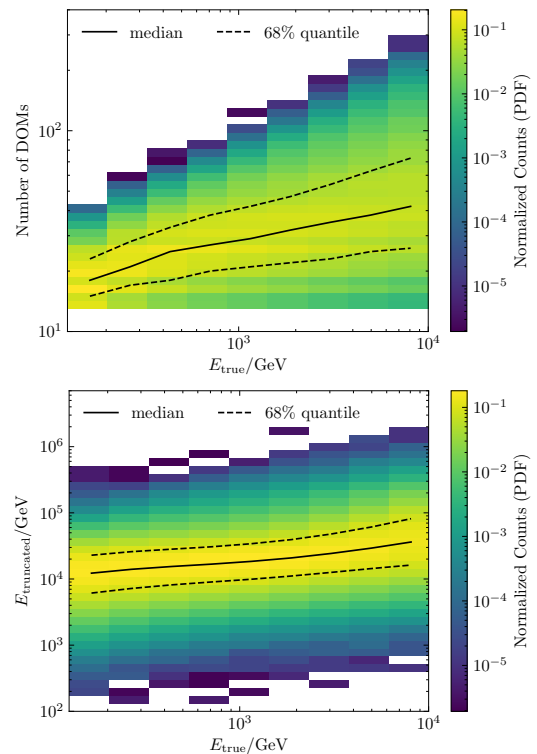


Fig. 7 Correlation between energy proxies and simulated neutrino energy. The events are normalized to the total number of counts in the simulated dataset per column, binned according to true neutrino energy, as used in the analysis.

Since the unfolding algorithm is trained on simulated events, a good agreement between the shape of simulated and experimental data is required for the energy proxies. For algorithm training and comparing data and simulation, simulated events are weighted to a realistic flux scenario for atmospheric and astrophysical neutrino flux of muon neutrinos. The atmospheric flux assumption is provided by MCEq, with H3a as the primary composition, SIBYLL-2.3c as the hadronic interaction model, and NRLMSISE-00 as the atmospheric model for the annual average, as selected for the calculation shown in Fig. 4. The astrophysical flux assumption is adopted from [28].

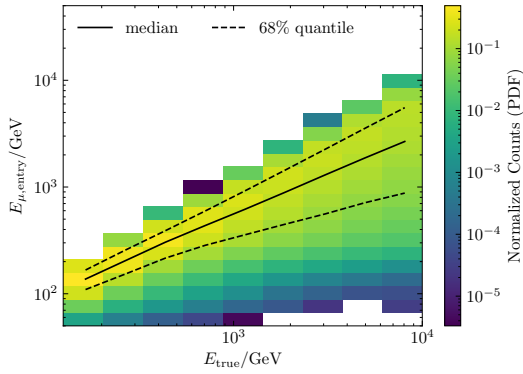


Fig. 8 The correlation between the true muon energy at detector entry to the true neutrino energy. This smeared correlation is attributed to the unknown distance between the detector and the position of muon production, highlighting the complexity of accurately reconstructing neutrino energy from measured quantities.

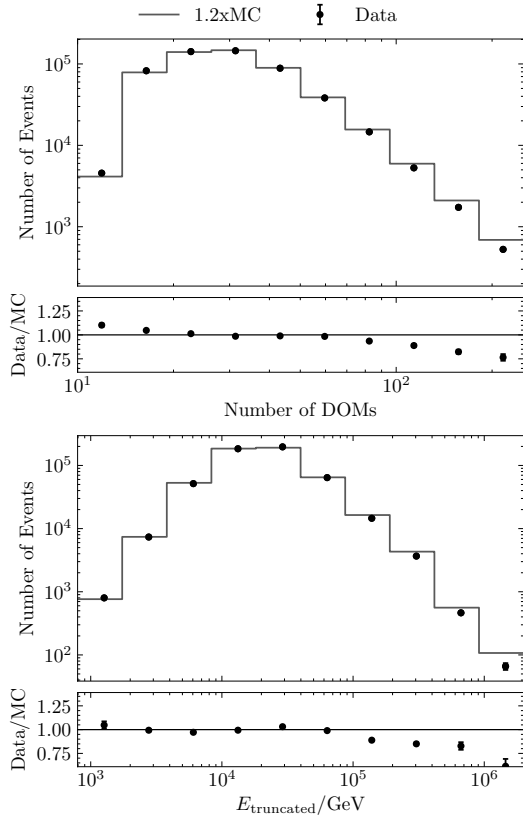


Fig. 9 Data-MC agreement for both energy proxies used in unfolding. The distribution of simulated events is normalized to the number of events in the data set by a normalization factor of 1.2. The top figure shows the proxy variable *number of DOMs*, and the bottom figure shows the energy proxy *truncated energy*.

Fig. 9 shows the agreement between data and weighted simulation for both energy proxies. The distribution of simulated events is normalized to the total number of events in the dataset, resulting in a scaling factor of 1.2. The upper panel depicts the number of events per bin, including statistical uncertainties, while the lower panel shows the ratio between the two. The distribution of simulated events generally agrees with experimental data within statistical uncertainties, except for deviations observed in the number of DOMs above 100, and above 1×10^5 GeV for $E_{\text{truncated}}$. These respective ranges correspond to neutrino energies outside of the analyzed range below 10 TeV, as can be inferred from Fig. 7.

The measurement of seasonal variations is robust against potential constant offsets in the distribution of simulated to experimental data since the measurement is performed relatively to the annual average flux, as further detailed in Section 6.

The algorithm is trained on the yearly average neutrino flux prediction and does not obtain any information on seasonal flux modulation. The robustness against deviations in the spectral index of the annual average to the training spectrum is tested, as described in Appendix B. The energy spectrum is unfolded into ten logarithmically equidistant energy bins from 125 GeV to 10 TeV.

5.3 Systematic and statistical uncertainties

Systematic uncertainties in the unfolded spectrum arise from various sources, including the detector uncertainties, detector medium, and reconstruction process. Each systematic uncertainty is assessed through simulated events, whereby pseudo-samples are unfolded by varying one parameter at a time. This approach is consistent with previous uncertainty estimations in spectrum unfolding (e.g., [35, 36, 37]).

Specific uncertainties include those from quantum efficiency of the optical modules (σ_{DOM}), ice absorption (σ_{abs}), scattering (σ_{scat}), optical properties of the refrozen ice around cable strings ($\sigma_{\text{hole ice}}$). These uncertainties are consistently calculated using variations of $\pm 10\%$ for DOM efficiency, $\pm 5\%$ for absorption and scattering, and polynomial function approximations for the hole ice [38, 27]. The flux uncertainties from hadronic interaction and primary cosmic-ray composition (σ_{flux}) are determined from parameterizing the results from [39], accounting for changes in the spectral shape. The uncertainty associated with deviations from the true distribution in unfolded pseudo-samples ($\sigma_{\text{DSEA+}}$) is accounted for by constraining it as a constant systematic uncertainty of $\pm 5\%$ across all energy bins (see Fig. 13 in Appendix B). The total uncertainty per energy

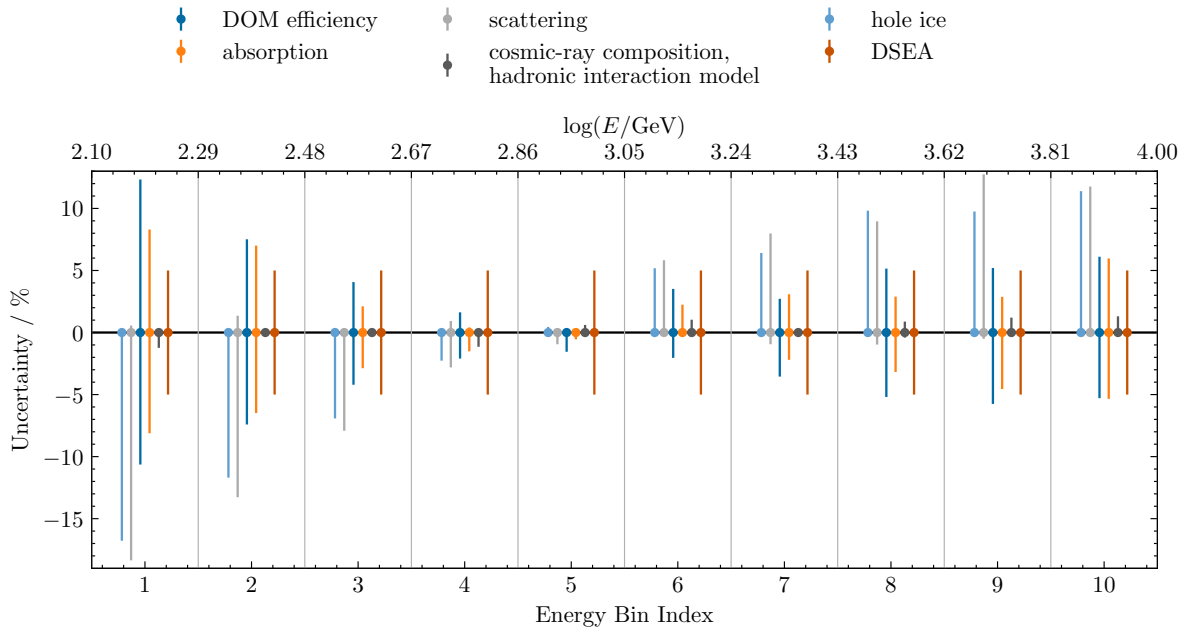


Fig. 10 A detailed overview of systematic uncertainties of the unfolded spectrum is provided per uncertainty type and energy bin. The systematic uncertainty remains constant across all seasons, as it is determined relatively to the reference simulation. The asymmetry of the uncertainties arises from the unfolding of pseudo data generated from simulations with altered systematic parameters, which have a larger effect on energy bins with smaller statistics.

bin is computed relative to the reference simulation, with upper and lower uncertainties assessed separately, summing all deviations in quadrature.

Fig. 10 shows the impact of each systematic uncertainty on the unfolded spectrum per energy bin, with larger uncertainties at the edges of the samples due to limited statistics. Asymmetric uncertainties arise because the variation of a single parameter in the simulation does not yield a linear response in the unfolded spectrum. These systematic uncertainties are seasonally independent as they arise from the in-ice detector, reconstruction and the data analysis pipeline.

Statistical uncertainties are determined using a bootstrap approach, in which the dataset is sampled in 2000 trials and unfolded. Each sample is generated by randomly drawing events from the original dataset, allowing the same event to be selected more than once within a single sample. This procedure creates 2000 independent pseudo-samples that reflect the statistical distribution of the original dataset. The standard deviation of the unfolded number of events per bin serves as the measure of statistical uncertainty for the unfolded spectrum. The total and statistical uncertainties are listed in Table 2 of the Appendix A.2.

6 Seasonal variations in the unfolded spectrum

The unfolded event spectra are converted to a differential flux by accounting for the livetime of the seasonal datasets, the effective area of the event selection determined from the detector response simulation, and the solid angle. Fig. 11 depicts the unfolded energy spectra corresponding to Austral summer (October to January) and winter (May to August) for the zenith range from 90° to 110° . The left panel shows the unfolded seasonal spectra along with the corresponding statistical and systematic uncertainties, compared to MCEq with H3a as the primary composition, SIBYLL-2.3c as the hadronic interaction model, and NRLMSISE-00 as the atmospheric model, as well as to daemonflux [40]. Daemonflux utilizes the MCEq framework, here using NRLMSISE-00 as atmospheric parameterization, to calculate fluxes from calibrated muon data, employing the data-driven hadronic interaction model DDM [41] and the Global Spline Fit cosmic-ray composition model [42].

The unfolded seasonal spectra agree in shape with MCEq and daemonflux predictions within systematic uncertainties. Although, a detailed comparison of the unfolded annual average to both models reveals an excess in the data, as further detailed in Fig. 12 in Appendix A.2, the ratios remain unaffected by normalization off-

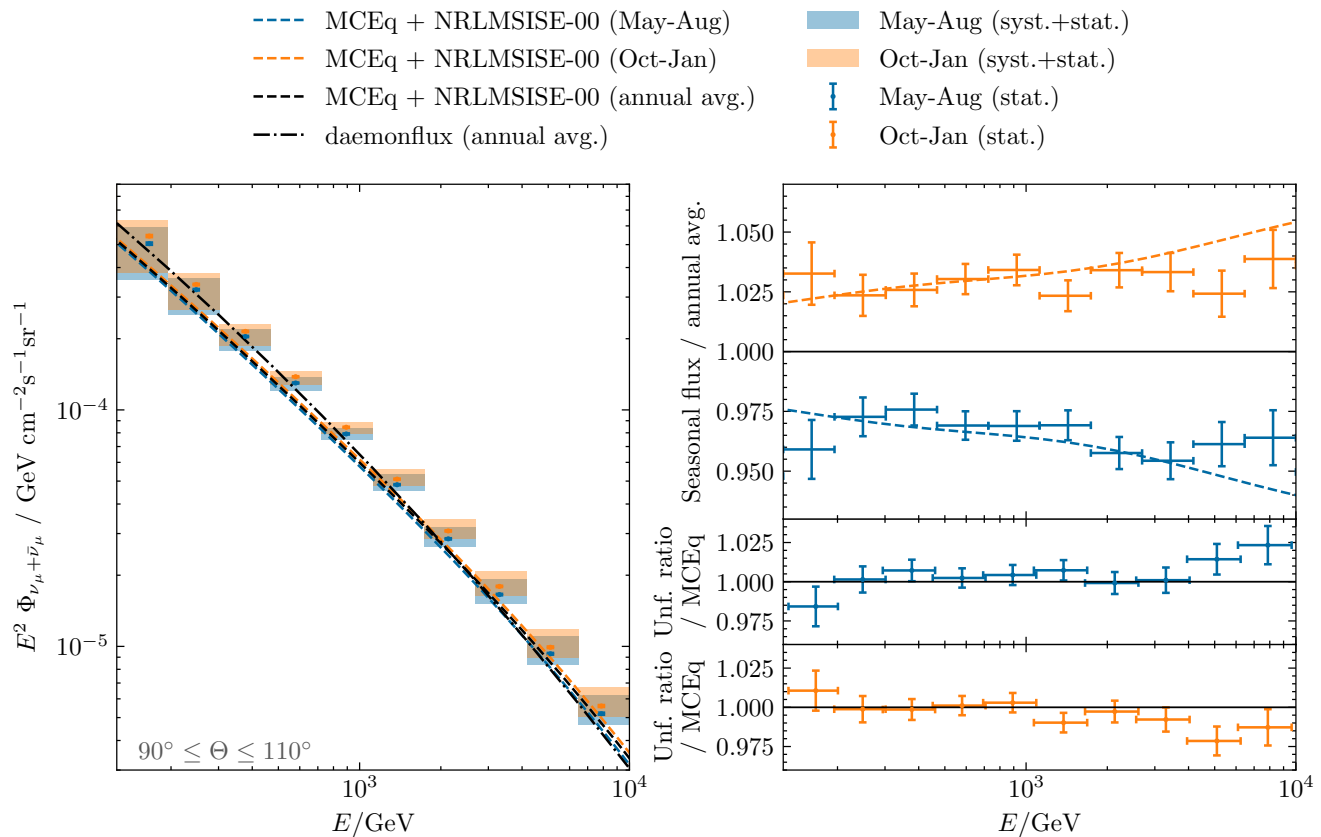


Fig. 11 The left panel shows the unfolded seasonal fluxes for Austral summer (October to January) and Austral winter (May to August) in the zenith range from 90° to 110° . Statistical uncertainties are depicted as error bars, while systematic uncertainties are represented as shaded areas. The theoretical predictions from MCEq (H3a, SIBYLL-2.3c, NRLMSISE-00) and daemonflux are shown in dashed and dash-dotted lines, respectively. The upper half on the right presents the ratio of the unfolded seasonal datasets to the annual average, indicating the seasonal variation strength across the energy range of interest. The systematic uncertainties remain constant for each season and cancel in the calculated ratio, leaving only statistical uncertainties to be shown. The lower half on the right displays the deviation of the unfolded ratio of the seasonal fluxes to the annual average with respect to the MCEq predictions for the ratio.

sets, as all seasons exhibit a consistent excess relative to the models.

The upper half on the right in Fig. 11 shows the ratio of unfolded seasonal fluxes to the annual average. As discussed in Section 5.3, systematic uncertainties cancel out in this relative measurement, leaving only statistical uncertainties in the measurement of the seasonal variation strength. The lower half on the right shows how the ratio of the unfolded seasonal fluxes to the annual average compares to MCEq predictions.

As expected, the amplitude of deviation of the seasonal to annual average flux increases with energy despite upward fluctuations in the first energy bin. During Austral summer, the rate variation rises from $(+2.3 \pm 0.9)\%$ in the second energy bin (above 194 GeV) to $(+3.9 \pm 1.2)\%$ (above 7 TeV). In contrast, during Austral winter, these ratios decrease from $(-3.3 \pm 0.8)\%$ to $(-4.6 \pm 1.1)\%$ (from energy bin 2 to 10, as shown in

Fig. 11). Table 1 in the Appendix A.1 lists the seasonal variation amplitude per energy bin.

The agreement between the unfolded seasonal-to-annual flux ratio and MCEq predictions with the NRLMSISE-00 atmospheric model is evaluated using a χ^2 -test. The p-values of 52.5% for May-August and 43.8% for October-January indicate the consistency of the observed seasonal variation strength with model predictions within the 1σ region. The choice of the hadronic interaction model has an impact on the spectral shape, but only a negligible impact on the seasonal variations below 10 TeV, which is purely driven by the atmospheric parameterization.

7 Conclusion and prospects

This study presents an energy-dependent measurement of seasonal variations in the atmospheric muon neutrino spectrum within the zenith range from 90° to 110° ,

covering energies from 125 GeV to 10 TeV. A previous measurement of the seasonal variation amplitude of atmospheric neutrinos from 6 years of IceCube data within the zenith range $90^\circ \leq \theta \leq 115^\circ$ reported an amplitude of $\pm 3.5(3)\%$, which is in tension with model predictions of $\pm 4.3\%$ using the AIRS atmospheric parametrization [16]. Building upon this prior work, our findings indicate a seasonal variation amplitude of $(-3.5 \pm 0.2)\%$ during the Austral winter (May to August) and $(+3.0 \pm 0.2)\%$ during the Austral summer (October to January), averaged over the analyzed energy range. These results exhibit a comparable tension of 2.7σ with ECMWF temperature data, increasing to 3.1σ and 4.6σ for AIRS data and the atmospheric model NRLMSISE-00, respectively.

The energy-dependent analysis shows that the strength of seasonal variation increases from May to August, reaching $(+3.9 \pm 1.2)\%$, and decreases from October to January to $(-4.6 \pm 1.1)\%$ relative to the annual average. This energy dependence stems from changes in atmospheric density gradients that influence production altitudes and the shift from pion-to kaon-dominated production. The unfolded seasonal variations in the energy spectrum align well with MCEq model predictions, using H3a as the cosmic-ray composition model, SIBYLL-2.3c for hadronic interactions, and the model NRLMSISE-00 for atmospheric conditions. While tensions are observed in the comparison of the observed rate variation with the MCEq prediction, no significant tension was found in the energy-dependent analysis for Austral summer and winter data. Discrepancies in rate variations relative to model predictions may arise from rapid temperature transitions during spring and fall, consistent with the findings in [16]. This study highlights neutrinos as a unique probe for exploring variations in the Antarctic atmosphere and the reliability of flux calculations with atmospheric models to describe the summer and winter seasons.

While the unfolded flux normalization within 90° to 110° is up to 30% higher than MCEq and daemonflux predictions, the differential seasonal variation measurements remain robust due to the cancellation of normalization uncertainties. This relative measurement allows to investigate the atmospheric neutrino flux in a regime often limited by significant modeling and measurement uncertainties.

Due to statistical limitations of the present dataset, the construction of seasonal datasets is based on averaging months with similar rate variations. For the same reason, seasonal unfolding above 10 TeV is currently not feasible, preventing conclusions about a prompt component in the atmospheric neutrino flux or astrophysical neutrinos at comparable energies. Both are unaffected by seasonal variations and would reduce the observed

amplitude for energies above the present range. Future analyses may investigate energy-dependent variations using a combination of atmospheric muons and muon neutrinos to measure a prompt component. The currently ongoing IceCube Upgrade [43] and IceCube-Gen2 expansion [44] will enhance model comparison capabilities by further reducing statistical and systematic uncertainties.

Acknowledgements The IceCube Collaboration acknowledges the significant contributions to this manuscript by Karolin Hymon. The authors gratefully acknowledge the support from the following agencies and institutions: USA – U.S. National Science Foundation-Office of Polar Programs, U.S. National Science Foundation-Physics Division, U.S. National Science Foundation-EPSCoR, U.S. National Science Foundation-Office of Advanced Cyberinfrastructure, Wisconsin Alumni Research Foundation, Center for High Throughput Computing (CHTC) at the University of Wisconsin–Madison, Open Science Grid (OSG), Partnership to Advance Throughput Computing (PATH), Advanced Cyberinfrastructure Coordination Ecosystem: Services & Support (ACCESS), Frontera computing project at the Texas Advanced Computing Center, U.S. Department of Energy-National Energy Research Scientific Computing Center, Particle astrophysics research computing center at the University of Maryland, Institute for Cyber-Enabled Research at Michigan State University, Astroparticle physics computational facility at Marquette University, NVIDIA Corporation, and Google Cloud Platform; Belgium – Funds for Scientific Research (FRS-FNRS and FWO), FWO Odysseus and Big Science programmes, and Belgian Federal Science Policy Office (Belspo); Germany – Bundesministerium für Bildung und Forschung (BMBF), Deutsche Forschungsgemeinschaft (DFG), Helmholtz Alliance for Astroparticle Physics (HAP), Initiative and Networking Fund of the Helmholtz Association, Deutsches Elektronen Synchrotron (DESY), and High Performance Computing cluster of the RWTH Aachen; Sweden – Swedish Research Council, Swedish Polar Research Secretariat, Swedish National Infrastructure for Computing (SNIC), and Knut and Alice Wallenberg Foundation; European Union – EGI Advanced Computing for research; Australia – Australian Research Council; Canada – Natural Sciences and Engineering Research Council of Canada, Calcul Québec, Compute Ontario, Canada Foundation for Innovation, WestGrid, and Digital Research Alliance of Canada; Denmark – Villum Fonden, Carlsberg Foundation, and European Commission; New Zealand – Marsden Fund; Japan – Japan Society for Promotion of Science (JSPS) and Institute for Global Prominent Research (IGPR) of Chiba University; Korea – National Research Foundation of Korea (NRF); Switzerland – Swiss National Science Foundation (SNSF).

References

1. T.K. Gaisser, R. Engel, E. Resconi, *Cosmic Rays and Particle Physics: 2nd Edition* (Cambridge University Press, 2016)
2. P.H. Barrett, L.M. Bollinger, G. Cocconi, Y. Eisenberg, K. Greisen, *Rev. Mod. Phys.* **24**(3), 133 (1952). DOI 10.1103/RevModPhys.24.133
3. S. Sagisaka, *Nuovo Cim. C* **9**, 809 (1986). DOI 10.1007/BF02558081

4. M. Ambrosio, et al., *Astropart. Phys.* **7**, 109 (1997). DOI 10.1016/S0927-6505(97)00011-X
5. A. Bouchta, in *26th International Cosmic Ray Conference* (1999). URL <https://articles.adsabs.harvard.edu/pdf/1999ICRC...2..108B>
6. P. Adamson, et al., *Phys. Rev. D* **90**, 012010 (2014). DOI 10.1103/PhysRevD.90.012010
7. S. Tilav, P. Desiati, T. Kuwabara, D. Rocco, F. Rothmaier, M. Simmons, H. Wissing, in *31st International Cosmic Ray Conference* (2010)
8. T. Abrahão, et al., *JCAP* **02**, 017 (2017). DOI 10.1088/1475-7516/2017/02/017
9. N. Agafonova, et al., *JCAP* **10**, 003 (2019). DOI 10.1088/1475-7516/2019/10/003
10. M. Agostini, et al., *JCAP* **02**, 046 (2019). DOI 10.1088/1475-7516/2019/02/046
11. E.W. Grashorn, J.K. de Jong, M.C. Goodman, A. Habig, M.L. Marshak, S. Mufson, S. Osprey, P. Schreiner, *Astropart. Phys.* **33**, 140 (2010). DOI 10.1016/j.astropartphys.2009.12.006
12. S. Verpoest, D. Soldin, P. Desiati, *Astropart. Phys.* **161**, 102985 (2024). DOI 10.1016/j.astropartphys.2024.102985
13. A. Fedynitch, F. Riehn, R. Engel, T.K. Gaisser, T. Stanev, *Phys. Rev. D* **100**, 103018 (2019). DOI 10.1103/PhysRevD.100.103018
14. G.D. Barr, T.K. Gaisser, S. Robbins, T. Stanev, *Phys. Rev. D* **74**, 094009 (2006). DOI 10.1103/PhysRevD.74.094009
15. A. Fedynitch, H. Dembinski, R. Engel, T.K. Gaisser, F. Riehn, T. Stanev, *PoS ICRC2017*, 1019 (2018). DOI 10.22323/1.301.1019
16. R. Abbasi, et al., *Eur. Phys. J. C* **83**(9), 777 (2023). DOI 10.1140/epjc/s10052-023-11679-5
17. M. Ackermann, E. Bernardini, in *29th International Cosmic Ray Conference* (2005)
18. P. Heix, S. Tilav, C. Wiebusch, M. Zöcklein, *PoS ICRC2019*, 465 (2020). DOI 10.22323/1.358.0465
19. A. Fedynitch, R. Engel, T.K. Gaisser, F. Riehn, T. Stanev, *EPJ Web Conf.* **99**, 08001 (2015). DOI 10.1051/epjconf/20159908001
20. T.K. Gaisser, *Astropart. Phys.* **35**, 801 (2012). DOI 10.1016/j.astropartphys.2012.02.010
21. F. Riehn, R. Engel, A. Fedynitch, T.K. Gaisser, T. Stanev, *Phys. Rev. D* **102**(6), 063002 (2020). DOI 10.1103/PhysRevD.102.063002
22. J. Picone, A. Hedin, D. Drob, A. Aikin, *Journal of Geophysical Research* **107** (2002). DOI 10.1029/2002JA009430
23. I.S.T. Teixeira. IRS/Aqua L3 Daily Standard Physical Retrieval (AIRS-only) 1 degree x 1 degree V006, Greenbelt, MD, USA, Goddard Earth Sciences Data and Information Services Center (GES DISC). DOI 10.5067/Aqua/AIRS/DATA303. URL https://acdisc.gesdisc.eosdis.nasa.gov/data/Aqua_AIRS_Level3/AIRS3STD.006/
24. H. Hersbach, B. Bell, P. Berrisford, G. Biavati, A. Horányi, J. Muñoz Sabater, J. Nicolas, C. Peubey, R. Radu, I. Rozum, D. Schepers, A. Simmons, C. Soci, D. Dee, J.N. Thépaut. Era5 hourly data on single levels from 1940 to present. Copernicus Climate Change Service (C3S) Climate Data Store (CDS) (2023). DOI 10.24381/cds.adbb2d47
25. A. Lecouffe, S. Godin-Beekmann, A. Pazmiño, A. Hauchecorne, *Atmospheric Chemistry & Physics* **22**, 4187 (2022). DOI 10.5194/acp-22-4187-2022
26. J.B. Stettner, Measurement of the energy spectrum of astrophysical muon-neutrinos with the icecube observatory. Phd thesis, RWTH Aachen University (2021). DOI 10.18154/RWTH-2021-01139. URL <https://publications.rwth-aachen.de/record/811376/files/811376.pdf>
27. M.G. Aartsen, et al., *JINST* **12**, P03012 (2017). DOI 10.1088/1748-0221/12/03/P03012. [Erratum: *JINST* **19**, E05001 (2024)]
28. R. Abbasi, et al., *Astrophys. J.* **928**, 50 (2022). DOI 10.3847/1538-4357/ac4d29
29. M.G. Aartsen, et al., *Astrophys. J.* **833**, 3 (2016). DOI 10.3847/0004-637X/833/1/3
30. K. Hymon, et al., *PoS ICRC2023*, 993 (2023). DOI 10.22323/1.444.0993
31. I. Fredholm, *Acta Math.* **27**, 365 (1903). DOI 10.1007/BF02421317
32. J.H. Koehne, K. Frantzen, M. Schmitz, T. Fuchs, W. Rhode, D. Chirkin, J. Becker Tjus, *Comput. Phys. Commun.* **184**, 2070 (2013). DOI 10.1016/j.cpc.2013.04.001
33. T. Ruhe, T. Voigt, M. Wornowizki, M. Borner, W. Rhode, K. Morik, in *Astronomical Data Analysis Software and Systems XXVI, Astronomical Society of the Pacific Conference Series*, vol. 521, ed. by M. Molinaro, K. Shortridge, F. Pasian (2019), *Astronomical Society of the Pacific Conference Series*, vol. 521, p. 394. URL <https://ui.adsabs.harvard.edu/abs/2019ASPC..521..394R>
34. R. Abbasi, et al., *Nucl. Instrum. Meth. A* **703**, 190 (2013). DOI 10.1016/j.nima.2012.11.081
35. M.G. Aartsen, et al., *Eur. Phys. J. C* **75**, 116 (2015). DOI 10.1140/epjc/s10052-015-3330-z
36. M.G. Aartsen, et al., *Eur. Phys. J. C* **77**, 692 (2017). DOI 10.1140/epjc/s10052-017-5261-3
37. A. Albert, et al., *Phys. Lett. B* **816**, 136228 (2021). DOI 10.1016/j.physletb.2021.136228
38. M.G. Aartsen, et al., *Nucl. Instrum. Meth. A* **711**, 73 (2013). DOI 10.1016/j.nima.2013.01.054
39. A. Fedynitch, J. Becker Tjus, P. Desiati, *Phys. Rev. D* **86**, 114024 (2012). DOI 10.1103/PhysRevD.86.114024
40. J.P. Yañez, A. Fedynitch, *Phys. Rev. D* **107**(12), 123037 (2023). DOI 10.1103/PhysRevD.107.123037
41. A. Fedynitch, M. Huber, *Phys. Rev. D* **106**, 083018 (2022). DOI 10.1103/PhysRevD.106.083018
42. H.P. Dembinski, R. Engel, A. Fedynitch, T. Gaisser, F. Riehn, T. Stanev, *PoS ICRC2017*, 533 (2018). DOI 10.22323/1.301.0533
43. A. Ishihara, *PoS ICRC2019*, 1031 (2021). DOI 10.22323/1.358.1031
44. M.G. Aartsen, et al., *J. Phys. G* **48**, 060501 (2021). DOI 10.1088/1361-6471/abbd48

Appendix A: Supplementary Material

Appendix A.1: Unfolded seasonal variation amplitude

The unfolded seasonal variation amplitudes per energy bin for Austral summer and winter and corresponding statistical uncertainties are listed in Table 1.

Appendix A.2: Unfolded annual average muon neutrino flux

The unfolded annual average flux used for the calculation of the seasonal variation strength in Fig. 11 and corresponding statistical and systematic uncertainties are summarized in Table 2. The comparison of the unfolded annual average flux to MCEq and daemonflux from Fig. 11 is displayed in Fig. 12. The shaded areas depict statistical and systematic uncertainties. The left panel showing the comparison to daemonflux takes into account additional systematic uncertainties from the data-driven model derivation.

Appendix B: Testing the unfolding method on pseudo-data

As a methodological test study, in addition to an annual average sample, two seasonal pseudo-samples are created, representing the summer and the winter, each containing the same number of events as expected during the data-taking period by weighting simulated events to the respective seasonal predictions from MCEq.

The training spectrum consists of simulated neutrino events in the zenith range from 90° to 120° , whereas the

pseudo-sample covers the zenith range from 90° to 110° only. As discussed in [30], the zenith range was restricted due to the lack of seasonal temperature variations in the atmosphere at zenith angles beyond 110° . The unfolding of the pseudo-samples ensures that the restricted range can be unfolded, and the seasonal variation strength can be obtained without the necessity to retrain the algorithm on the restricted range.

The left panel in Fig. 13 displays the ratio of the unfolded seasonal samples to the annual average to the true distribution of the pseudo-sample. Despite outliers in the first energy bin, the spectra can be retained in unfolding up to a deviation of $(3 \pm 1)\%$. Since the unfolded distributions for Austral summer and winter show a similar bias to the true spectrum, the unfolding error cancels out in the ratio of the seasonal sub-samples to the annual average flux. The uncertainty of the unfolded spectrum arising from the unfolding method is estimated by an upper bound of $\pm 5\%$, as depicted in Fig. 10.

The right panel depicts the ratio between the unfolded seasonal and the annual average. The unfolded seasonal variation strength, shown as the seasonal to annual average flux ratio, is consistent with the predicted ratios from MCEq for both seasons. With a p-value of 78.1% for the Austral winter from May to August and a p-value of 67.0% for Austral summer from October to January, the χ^2 -test indicates an agreement with the null-hypothesis (calculated seasonal flux variation from MCEq) within the 1σ region. It is only affected by statistical uncertainties since detector systematic uncertainties cancel out in the ratio. Nonetheless, systematic uncertainties are added to the unfolded spectrum.

Table 1 Unfolded seasonal variation amplitude for Austral winter (May to August) and Austral summer (October to January) across the energy range.

Season	Energy Bin Index									
	1	2	3	4	5	6	7	8	9	10
May-Aug	-4.1%	-3.3%	-2.4%	-2.7%	-3.8%	-3.5%	-3.0%	-3.5%	-4.6%	-4.6%
±	1.2%	0.8%	0.7%	0.6%	0.6%	0.6%	0.7%	0.8%	0.9%	1.1%
Oct-Jan	+4.1%	+2.3%	+2.8%	+3.0%	+3.1%	+3.6%	+1.7%	+3.4%	+2.7%	+3.9%
±	1.3%	0.9%	0.7%	0.6%	0.6%	0.7%	0.7%	0.8%	1.0%	1.2%

Table 2 Unfolded annual average atmospheric muon neutrino flux in the zenith range from 90° to 110° , along with the corresponding statistical and systematic uncertainties.

Energy Bin Index	$\log(E/\text{GeV})$	Center energy	$\frac{d\phi}{dE}$ [$\text{GeV}^{-1} \text{cm}^{-2} \text{s}^{-1} \text{sr}^{-1}$]	Stat. Uncertainty	Total Uncertainty	
1	2.10 – 2.29	2.211	1.81×10^{-8}	$\pm 0.6\%$	-29.8%	+16.8%
2	2.29 – 2.48	2.397	5.18×10^{-9}	$\pm 0.4\%$	-21.5%	+12.2%
3	2.48 – 2.67	2.584	1.42×10^{-9}	$\pm 0.3\%$	-13.3%	+7.3%
4	2.67 – 2.86	2.771	3.89×10^{-10}	$\pm 0.3\%$	-7.3%	+5.9%
5	2.86 – 3.05	2.958	1.00×10^{-10}	$\pm 0.3\%$	-5.9%	+5.6%
6	3.05 – 3.24	3.146	2.57×10^{-10}	$\pm 0.3\%$	-5.9%	+10.7%
7	3.24 – 3.43	3.335	6.43×10^{-12}	$\pm 0.3\%$	-7.1%	+12.7%
8	3.43 – 3.62	3.543	1.57×10^{-12}	$\pm 0.3\%$	-8.6%	+16.0%
9	3.62 – 3.81	3.713	3.67×10^{-13}	$\pm 0.4\%$	-9.7%	+18.6%
10	3.81 – 4.00	3.903	8.57×10^{-14}	$\pm 0.6\%$	-10.0%	+20.1%

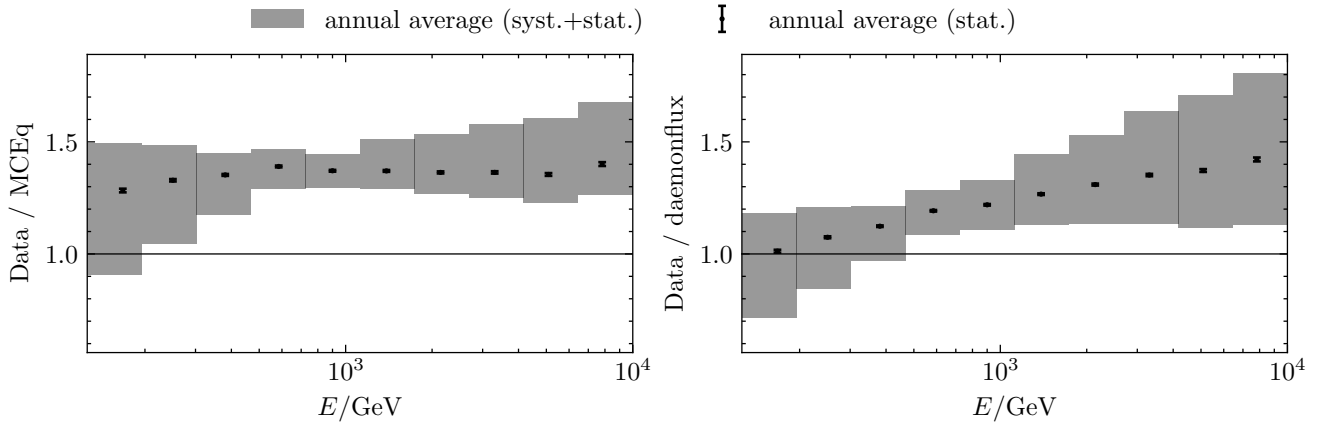


Fig. 12 Ratio of the unfolded annual average flux to model predictions. The left panel displays the comparison to MCEq with H3a, SIBYLL-2.3c, while the right panel compares it to daemonflux. The shaded areas depict the statistical and systematic uncertainties of the unfolded flux. Additional uncertainties for the daemonflux model are included in the right panel.

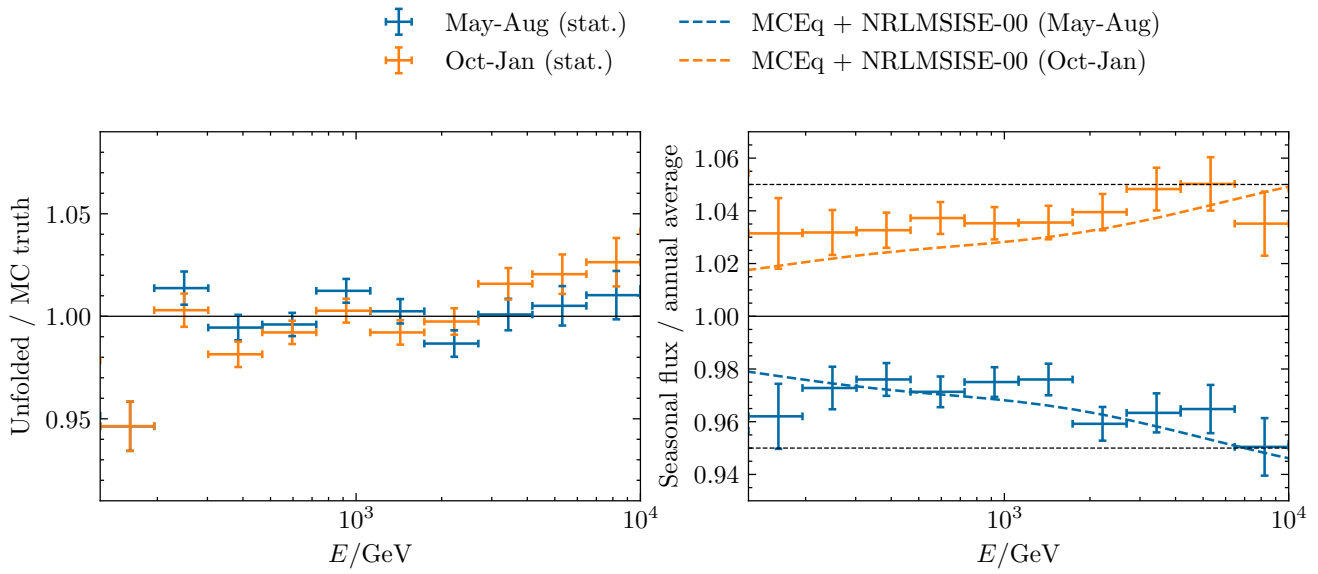


Fig. 13 The left panel shows the ratio of unfolded pseudo-samples of simulated neutrino events to the binned true event distribution corresponding to 11.3 years of experimental data, with statistical uncertainties depicted as error bars. The right panel shows the ratio of the unfolded seasonal pseudo-samples to the annual average. Dashed lines for the respective seasons represent the theoretical predictions from MCEq (H3a, SIBYLL-2.3c, NRLMSISE-00).